# Influence of Spheroidized Cementite on Ferritic Matrix Boundary Characteristics and Mechanical Behavior in Commercial Carbon Steels

**Mohammad Masoumi[a]\* ⓘ, M.A. Mohtadi-Bonab[b], Rodrigo C.P. Loureiro[c], Jorge L. Cardoso[c] ⓘ,**

**Miloslav Béreš[c], Hamilton F.G. de Abreu[c]**

[a] *Universidade Federal do ABC, Centro de Engenharia, Modelagem e Ciências Sociais Aplicadas, 09210-580, Santo André, SP, Brasil.*
[b] *University of Bonab, Department of Mechanical Engineering, Bonab, Iran.*
[c] *Universidade Federal do Ceará, Departamento de Engenharia Metalúrgica e de Materiais, 60445-554, Fortaleza, CE, Brasil.*

This research investigates the effects of accelerated spheroidizing of cementite on the mechanical properties and microstructural characteristics of commercial steel grades (Fe-0.2C, Fe-0.5C, Fe-0.7C wt%), emphasizing the role of cold-rolling reduction followed by stress relief annealing. Utilizing SEM imaging, X-ray diffraction, and EBSD measurements, this study comprehensively examines how variations in carbon content influence hardness, dislocation density, and crystallographic texture orientation. Microhardness measurements reveal a direct relationship with carbon content, yielding values of 28.0±1.0 HRC for DT-1020, 36.0±1.0 HRC for DT-1050, and 39.0±1.0 HRC for DT-1070. Texture analysis through EBSD demonstrates distinct patterns among the grades: DT-1020 displays a dominant (111) texture, DT-1050 exhibits a (101) orientation, and DT-1070 features a more refined (101) texture. Dislocation density analysis further corroborates the impact of carbon content, with DT-1050 presenting the highest density at approximately $7.8 \times 10^{16}$ m$^{-2}$. This detailed exploration elucidates the intricate interplay between carbon content, cementite morphology, and their collective influence on mechanical performance of steel, providing valuable guidance for tailoring steel properties via microstructural control.

**Keywords:** *spheroidized cementite, role of misorientations, KAM data, <111> fiber textures.*

## 1. Introduction

Pearlite, a composite microstructure characterized by ferrite and lamellar cementite, is paramount in steels. Intense cold rolling of pearlite diminishes the interlamellar spacing and reduces the lamellar cementite thickness[1-3]. Following this, the annealing process plays a critical role in expediting the spheroidization of lamellae. It is important to note that spheroidization primarily aims to enhance the machinability of the material. This process involves the transformation of lamellar cementite into a spheroidal form, which is a time-consuming step due to the extended holding time required for this structural change. The result of this careful and deliberate process is the formation of microduplex structures comprising both ferrite and cementite phases. The transition from lamellar pearlite to these structures is documented extensively in the literature[4-7]. The driving force for this spheroidization, particularly in diverse steel types, is minimizing surface-free energy. This morphological shift from lamellar cementite to spherical formations not only enhances the mechanical resilience and ductility of the steel, as noted in references[8,9], but also significantly improves its cold-forming characteristics. It is important to highlight that the spheroidized microstructure effectiveness

in cold forming is influenced by the size and spacing of the spheroids; larger spheroids with greater distances between them tend to increase the steel ability to be cold-formed.

Spheroidized ferrite-cementite steel (SFC) has obtained attention due to its critical role in improving mechanical resilience and cold-forming characteristics of steels, a process that transforms lamellar cementite into spheroids to minimize surface-free energy and enhance ductility. Recent studies by Zhu et al.[10] emphasize the significance of accurately estimating residual stress levels and distributions in welded structures, as tensile residual stresses on surfaces or subsurfaces can exacerbate crack initiation and growth under cyclic loads, crucial for assessing the reliability of mechanical equipment. Concurrently, Wang et al.[11] delve into the susceptibility of SFC to micro-defects arising from the mismatched deformation between ferrite and cementite during cold forming. These micro-defects can significantly impair fatigue life, highlighting the necessity of understanding damage mechanisms related to microstructural features to better control the microstructure and forming processes. Through a combination of experiments and multiscale simulations, Fu et al.[12] identify cementite cracking, ferrite/cementite interface debonding, and ferrite cracking as primary damage mechanisms under uniaxial tension in SFC steel,

with interface debonding playing a dominant role in final fractures. This comprehensive approach aids in capturing the driving forces behind these mechanisms and the dependence on microstructural features, offering insights into optimizing the spheroidization process and enhancing the performance of SFC in industrial applications.

In previous studies[1,3,5,7], spheroidized cementite particles in steels have been predominantly identified as elliptical spheroids, maintaining an aspect ratio between 0.7 and 1.0. This ratio indicates the relationship between the minor and major axes of the spheroids. Advanced microstructural analyses utilizing FE-SEM and HR-EBSD techniques have unveiled spherical cementite structures predominantly located along high and low-angle grain boundaries[1,13]. Furthermore, the literature elucidates how spheroidization mechanisms, specifically the variations in stored energy, dictate the cementite dissolution rates in the initial spheroidization stages[14]. In contrast to prior studies, this research aims to elucidate the outcomes of an accelerated cementite spheroidization process achieved through subcritical annealing. Our work uniquely emphasizes the interplay between crystallographic texture and mechanical characteristics, striving to bridge existing gaps in understanding and application within steel research.

Recent studies have provided in-depth insights into the microstructural evolution in pearlitic steel samples, particularly focusing on the changes induced by cold rolling and annealing. It is important to recognize that the spheroidization process can be categorized into two distinct stages: the initial breaking of cementite lamellae and the subsequent coarsening of cementite particles. An alternative method to cold rolling is cyclic heat treatment, which might yield noteworthy results worth considering. Additionally, the complexity inherent in the fast spheroidization process lies in determining the optimal high temperature and suitable holding time to achieve the desired microstructural transformation. Furuhara et al.[2] unveiled the heterogeneous nature of cold-rolled pearlitic structures, categorizing them based on lamellar characteristics and observing the emergence of a microduplex structure upon annealing. This intricate response is further complicated when considering temperature-sensitive spheroidization processes, with Matusiewicz et al.[7] noting the significant role of coupled interface diffusion during spheroidization at varying annealing temperatures. Delving into the morphological intricacies, Amos et al.[5] employed phase-field modeling to discern capillary-mediated mechanisms that dictate spheroid formation, uncovering pivotal evolutionary shifts in cementite spheroidization, mainly based on aspect ratios. The profound impact of rolling methods on microstructure and texture was highlighted by Narayanswamy et al.[1], who revealed distinctive structural outcomes between unidirectional cold-rolling and cross-rolling, the latter being accompanied by pronounced shear bands and bent lamellae. Lastly, the intricate interplay between ferrite recrystallization, cementite behavior, and austenite transformation during annealing in Dual-Phase steels was emphasized by Teixeira et al.[3], underlining the multifaceted interdependencies within the cold-rolled ferrite-pearlite microstructure. While these studies provide foundational insights, our work delves deeper into the rapid cementite spheroidization process and its subsequent influence on mechanical properties.

The main goal of this research is to conduct an in-depth investigation into the impact of enhanced spheroidizing of cementite on the properties of selected commercial steel grades, with a spotlight on the cold-rolling reduction process as a pivotal factor. This study meticulously follows a specialized commercial treatment involving precise thermal management below and between critical temperatures ($Ac_1$ and $Ac_3$), coupled with controlled cooling, to modify the microstructure of steel. By employing advanced analytical techniques such as SEM imaging, X-ray diffraction, and EBSD measurements, we aim to explore the intricate relationship between the microstructure of steel, particularly the evolution of spheroidized cementite, and its mechanical performance indicators—strength, ductility, and energy absorption. This investigation is critical in understanding the influence of carbon content on these properties and identifying the balance between strength and ductility that is crucial for optimizing the performance of steel in manufacturing processes. Our research is distinguished by its focus on the symbiosis between crystallographic texture and mechanical properties, endeavoring to fill the knowledge gaps in steel research and application. Significantly, this study provides essential insights into tailoring steel production techniques for the spheroidization of cementite, offering substantial benefits across diverse industries reliant on pearlitic steel, such as automotive, construction, and defense sectors, where the demand for materials combining superior strength with enhanced ductility is paramount. Thus, this work not only contributes to the scientific understanding of steel microstructure and properties but also serves as a crucial resource for industry stakeholders aiming to enhance the performance and reliability of pearlitic steel in demanding applications.

## 2. Materials and Experimental Procedures

### 2.1. Materials used in this study

This study investigated the microstructural evolution of three different batches of commercially sourced carbon steels, specifically AISI and SAE grades 1020, 1050, and 1070. These steels, each with an initial thickness of 20 mm, are widely used in various industrial components. The chemical compositions of the samples were determined using an optical emission spectrometer (Shimadzu PDA 7000) and are presented in Table 1.

In our analysis of the AISI 1020, 1050, and 1070 steel samples, while we primarily focus on the influence of carbon content on their microstructure and mechanical properties, it is important to acknowledge the presence of other alloying elements such as Cu, Ni, Cr, Mo, Nb, etc. Though these elements are present in smaller quantities compared to carbon, they can still significantly influence the properties of steel. For instance, elements like Ni and Cr can enhance strength and corrosion resistance, while Mo and Nb can impact hardenability and grain refinement. Therefore, while our study predominantly concentrates on carbon due to its predominant role in defining the characteristics of steel, the effects of these additional elements, albeit minor, are also considered in the overall analysis of the material properties.

Influence of Spheroidized Cementite on Ferritic Matrix Boundary Characteristics and Mechanical Behavior in Commercial Carbon Steels

3

**Table 1.** Chemical compositions of the samples in (wt.-%).

| Specimen | C | Si | Mn | P | S | Ni | Cr | Mo | Cu | Nb | Ti | Fe |
|---|---|---|---|---|---|---|---|---|---|---|---|---|
| AISI 1020 | 0.22 | 0.23 | 0.73 | 0.010 | 0.004 | 0.027 | 0.030 | 0.013 | 0.014 | 0.007 | 0.003 | bal |
| AISI 1050 | 0.52 | 0.19 | 0.59 | 0.007 | 0.010 | 0.030 | 0.035 | 0.005 | 0.005 | 0.001 | 0.003 | bal |
| AISI 1070 | 0.77 | 0.20 | 0.50 | 0.006 | 0.008 | 0.016 | 0.024 | 0.006 | --- | --- | 0.001 | bal |

Each steel sample underwent identical processing, encompassing annealing, cold rolling, and stress relief annealing. The samples underwent initial homogenization at 950°C for one hour, followed by a carefully controlled air-cooling process critical for inducing pearlite transformation. The cooling rate is pivotal in determining the microstructure and hardness of the steel; slower cooling typically yields a softer, more spheroidic microstructure, whereas a faster rate favors a lamellar formation. The cold-rolling reduction was performed to accelerate the spheroidization kinetics of the pearlitic microstructure[15]. For the cold rolling, the annealed specimens were resized into rectangular plates measuring $200\times70\times20mm^3$, ensuring compatibility with the laboratory rolling machine (Mascote LE 110) equipped with rollers of 150 mm in working length and 70mm in diameter. The cold rolling process, conducted at room temperature, comprised two passes: the first reduced the sample thickness to 15 mm (a 25% reduction) and the second to 10mm (an additional 33.33% reduction). The true strains for these passes were 0.28768 and 0.40547, respectively, accumulating to a total true strain of 0.69315 over the entire process. To mitigate cold deformation effects like work hardening, anisotropy from grain elongation, and residual stress-induced cracking, the samples underwent annealing at 650°C for 30 minutes for stress relief, followed by air cooling. This specific annealing duration and temperature were chosen to balance ductility and strength, avoiding the risks of embrittlement associated with prolonged treatment. Cold-deformed and thermal-treated specimens are called DT-1020, DT-1050, and 1070 through the current manuscript.

## 2.2. Characterization techniques and experimental procedures

Microstructural evaluations were carried out on longitudinal sections employing FEI® Quanta 450 and FEI® Quanta 650 FEG-SEM systems equipped with Oxford Instruments EBSD detectors. The mean dimension of the spheroidized cementite was deduced from three SEM images through a methodical evaluation using the ImageJ® software. Specimens for the EBSD analysis were dimensioned to 10×10 mm on their RD-ND planes, followed by an initial grinding and manual polishing employing a 1 µm diamond compound. A subsequent 12-hour polish using 0.04 µm colloidal silica ensured an optimal surface for EBSD examination. All EBSD maps were acquired at a magnification of 2000 times and a step size of 500 nm. This specific magnification and step size were strategically selected to gather comprehensive data on grain distortion within the grains, thereby enabling a detailed analysis of the grain condition for each sample. By choosing these parameters, we aimed to ensure an optimal balance between data coverage and the resolution necessary to observe microstructural nuances accurately. The subsequent processing of the EBSD data was carried out using Oxford

Instruments Channel 5 and ATEX software[16], providing a robust framework for analyzing and interpreting the intricate details revealed by the EBSD maps. This meticulous approach to data collection and processing underpins our findings and contributes to a deeper understanding of the microstructural characteristics of the material.

Additionally, an X'Pert Pro PANalytical® XRD system, utilizing Co Ka rays ($\lambda = 1.7890100$ A˚) set at 45 kV and 45 mA, was engaged for detailed microstructural and textural analysis. Specimens destined for XRD assessment were dimensioned to 10×10 mm on their RD-ND planes and finely ground using #1200 grit paper.

The measurement of lattice parameters (a, b, and c) for a orthorhombic crystal structure ($a \neq b \neq c$) using X-ray diffraction (XRD) relied on Bragg's Law and the specific geometry of the crystal structure.

Bragg's Law states that a diffraction pattern occurs when X-rays are diffracted by the lattice planes of a crystal. The law is expressed as $n\lambda = 2d\sin\theta$, where n is the order of diffraction, $\lambda$ is the wavelength of the incident X-rays, d is the spacing between the lattice planes, and $\theta$ is the angle of incidence that results in diffraction. The spacing between the lattice planes (d) in a orthorhombic structure is given by the formula[17]:

$$1/d^2 = h^2/a^2 + k^2/b^2 + l^2/c^2$$

where (hkl) are the Miller indices of the plane causing diffraction.

So, given the angles of diffraction for the (110), (200), and (211) planes, the corresponding d-values using Bragg's Law can be calculated. The determined d-values are used in the formula above to derive a set of three equations. The unknowns are the lattice parameters a, b, and c.

$$1/d_1^2 = 1/a^2 + 1/b^2 \ \dots \quad \text{(Eq. 1) for (110)}$$

$$1/d_2^2 = 4/a^2 \ \dots \quad \text{(Eq. 2) for (200)}$$

$$1/d_3^2 = 4/a^2 + 1/b^2 + 1/c^2 \ \dots \quad \text{(Eq. 3) for (211)}$$

Where $d_1$, $d_2$, and $d_3$ are the interplanar distances corresponding to the (110), (200), and (211) planes, respectively, calculated from the diffraction angles using Bragg's Law.

These equations can be solved numerically to find the values of a, b, and c using a method such as Newton's method, or using a numerical solver in a software package such as MATLAB or Python SymPy module. This method assumes that the crystal is ideal and ignores factors such as thermal vibration, crystal defects, or instrumental errors, which could slightly alter the results.

Parameters like dislocation density, internal strain, and grain dimension were inferred from XRD outputs through the

combined utilization of the Debye – Scherer equation[18] and the Stokes-Wilson method[19]. The formula for dislocation density (δ) is represented as:

$$\delta = \frac{1}{t} \qquad \text{(Eq. 4)}$$

Here, t refers to the grain dimension related to the disparity between crystal entities and non-uniform deformation, as detailed in the Debye–Scherer equation[20,21]:

$$t = \frac{0.9 \times \lambda}{\beta_{(1/2)} \times cos\theta} \qquad \text{(Eq. 5)}$$

In this context, λ stands for ray wavelength, β(1/2) is the peak FWHM, and θ represents the angle of X-ray diffraction. The internal strain was deduced from the Stokes-Wilson equation[22]:

$$\varepsilon = \frac{\beta_{(1/2)}}{4 \times tan\theta} \qquad \text{(Eq. 6)}$$

Following the DIN EN 6892-1 standard[23], tensile test specimens, measuring 20 mm in gauge length were subjected to tensile tests at a deformation speed of 0.05mm/s. An AG100 uniaxial testing machine was utilized for tensile tests, and the results are illustrated as engineering stress-strain plots.

## 3. Results and Discussion

### 3.1. Microstructural variations and Carbide Spheroidization in DT-Series Steels

Observations from the SEM micrographs presented in Figure 1 underscore the influence of mechanical and thermal treatment on the microstructure of the three steel specimens: DT-1020, DT-1050, and DT-1070. The spheroidized carbide precipitates, distributed in the ferritic matrix and at grain boundaries, manifest the prevalent effects of the treatments on these steels. For the DT-1020 specimen, the spheroidized carbide particles fall within an average size range from 200 to 300 nm. This is consistent with the trends reported by Li et al.[24] who noticed the spheroidization of cementite upon annealing, particularly at higher temperatures. The thermal treatment might have accelerated the spheroidization process, fostering the dissolution of lamellae and consequently aiding the spheroidization of cementite lamellae[25].

The DT-1050 sample also showcases spheroidized carbide particles within the same size range. However, the presence of cell structures indicates localized deformation regions. As noted by Narayanswamy et al.[1], such deformation heterogeneities as kinks can be pivotal in accelerating the spheroidization process during annealing, leading to inhomogeneous diffusion of carbon due to the chemical potential difference. This could be linked to the carbon distribution within the pearlitic matrix and differences in thermally activated diffusion within the grains and at grain boundaries, aiming to minimize the interfacial energy[26]. The higher temperature might have also augmented the role of kinks in enhancing spheroidization.

Conversely, the DT-1070 specimen exhibited the finest cementite particles interspersed within the ferritic matrix. This can be attributed to the higher carbon content, which inherently influences the cementite fraction in the sample. Zhao et al.[9] elucidated that with increased holding time, pearlitic structures undergo spheroidization, leading to the lamellar structure disappearance and causing carbide to distribute along the grain boundaries. Given the higher carbon content in DT-1070, the propensity for carbide formation is increased, leading to finer and more abundant cementite particles.
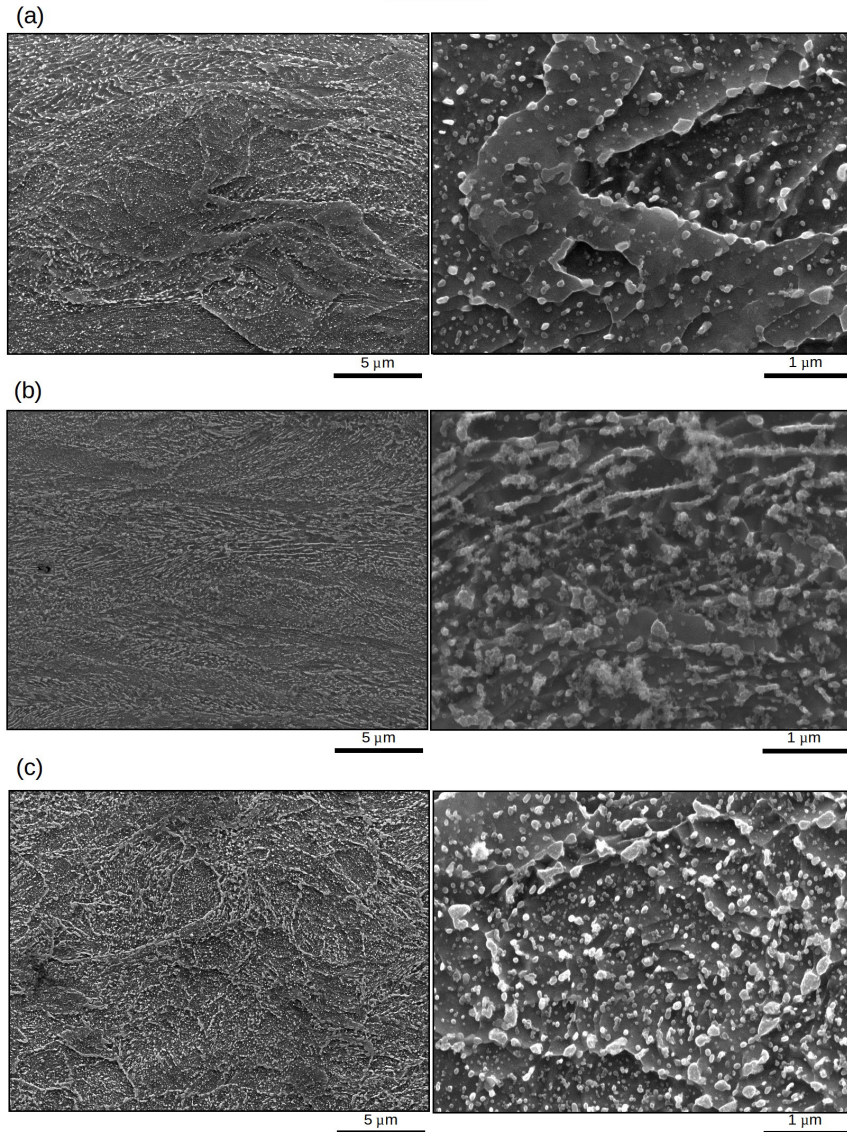
Furthermore, the observed differences in carbide morphology across the specimens highlight the intertwined relationship between mechanical and thermal treatments, as well as the inherent carbon content of the steel. Li et al.[24] pointed out that the strength of pearlitic structures, contingent on the cell/subgrain structures in the ferrite, can witness coarsening, leading to microstructural softening[27]. This coarsening, intertwined with the mechanical and thermal histories of the specimens, is evident in the distinct morphologies captured in Figure 1.

### 3.2. Carbon, Cementite Morphology, and Microhardness in DT Steels

The microhardness tests on DT-1020, DT-1050, and DT-1070 specimens showcased a direct correlation between hardness values and carbon content, registering at 28.0±1.0 HRC, 36.0±1.0 HRC, and 39.0±1.0 HRC, respectively. The elevated hardness with increased carbon content, as observed in DT-1070, is due to the increased concentration of carbon atoms that have a pinning effect, impeding dislocation motion. This trend is further accentuated in the DT-1050 sample. However, it shares a similar particle size range as DT-1020, and its cell cementite structures provide more complex barriers to dislocation movement than the uniformly spheroidized particles of DT-1020[28]. Meanwhile, the DT-1070 enhanced hardness can be attributed to its finer cementite particles, increasing the particle-matrix interfaces, and superior carbon content.

The Hall-Petch equation underscores that yield strength (and hardness) is inversely proportional to the square root of the grain size. Primarily framed within the context of matrix grain size, this principle can also extend to carbide precipitates, suggesting that finer precipitates are more effective in obstructing dislocation movement due to their increased density at particle-matrix interfaces. This principle helps elucidate the pronounced hardness in DT-1070, shaped by its minuscule cementite particles. In essence, the DT-series steels' hardness is an intricate balance between carbon content and the character of spheroidized cementite, both of which determine the mechanical resilience of material.

The initial observations of ferrite and cementite morphologies set the stage for understanding the complex interplay between microstructural elements and their mechanical implications. The presence of circular or elliptical cementite particles within a ferrite matrix not only delineates the heterogeneous nature of the microstructure but also underscores the influence of carbon content and processing techniques on material properties. This heterogeneity is further evidenced by the variable strain distributions under tension, highlighting the non-uniform response of the material to mechanical loading[11]. The detailed

Influence of Spheroidized Cementite on Ferritic Matrix Boundary Characteristics and Mechanical Behavior in Commercial Carbon Steels

5



**Figure 1.** SEM SE micrographs of deformed and thermally treated (a) DT-1020, (b) DT-1050, and (c) DT-1070 specimens. Spheroidized carbide precipitates distributed in ferritic matrix and grain boundaries are visible.

analysis of void formation and growth mechanisms under tensile loading conditions reveals critical insights into the damage processes within spheroidized ferrite-cementite steel[12]. The identification of three primary damage mechanisms - ferrite/cementite interface debonding, cementite cracking, and ferrite cracking - provides a nuanced understanding of the factors leading to material failure. These mechanisms are intricately linked to the microstructural features, such as particle size and distribution, which in turn are influenced by carbon content of the steel and processing history[29].

## 3.3. Depth-dependent EBSD analysis of cold-rolled and annealed steels

When specimens were subjected to cold rolling followed by annealing, they experienced significant microstructural changes. Cold rolling increases dislocation density, grain elongation leading to deformation bands, especially in high carbon steels. Subsequent annealing can cause recovery and recrystallization. The microstructure at the sample surface might differ from the centre due to factors such as thermal gradients during annealing, uneven deformation during cold rolling, and surface effects like oxidation or decarburization. Thus, considering these factors, it is plausible for the microstructure of these specimens to exhibit variations from the surface to the middle of their thickness.

By analyzing both the surface (approximately 20μm below the surface) and the middle of the thickness of DT-1020, DT-1050, and DT-1070 steels using EBSD, taking a comprehensive approach to understanding the depth-dependent microstructural variations resulting from cold rolling and subsequent annealing processes. The normal direction orientation image map provides insights into

the crystallographic orientations relative to the rolling direction, revealing how the processing has affected texture development differently in the surface compared to the center of sample. Disorientation/reference orientation data will offer valuable information on the misorientations between grains, indicating the degree of deformation and potential recrystallization. The Entrywise Norm of the Nye Tensor, on the other hand, provides a quantification of geometrically necessary dislocations, giving clues about localized strain variations. Together, these techniques will not only unveil depth-dependent microstructural intricacies in each steel type but also highlight the influence of carbon content on grain and crystallographic variations, thereby providing a holistic view of the microstructural evolution in these materials.

### 3.3.1. Surface texture and dislocation dynamics by carbon content

Figure 2 presents the normal direction orientation image (OIM), disorientation/reference orientation, and the Entrywise norm of the Nye tensor maps for the DT-1020, DT-1050, and DT-1070 samples. The DT-1020 orientation image predominantly showcases a (111) texture, with its disorientation map highlighting variations between recrystallized and larger deformed grains, both exhibiting a (111) orientation. The Nye tensor map for DT-1020 delineates regions with

dislocation densities around $4.5 \times 10^{14}$ m$^{-2}$. In contrast, the DT-1050 orientation map is characterized by ferritic grains oriented parallel to the (101) plane, aligned with the rolling direction, interspersed with grains oriented along the (101) and occasional (001) planes. These (101) plane-aligned grains suggest dynamic recrystallization due to their low boundary angles, and there is noticeable impedance in dislocation motion near the (001) grains, with a resultant dislocation density of around $7.8 \times 10^{16}$ m$^{-2}$. The DT-1070 sample reveals a deformed and refined microstructure, predominantly featuring a (101) texture orientation, complemented by a balanced representation of distortion and dislocation accumulation in the disorientation map. The associated Nye tensor map indicates a dislocation density of approximately $4.6 \times 10^{16}$ m$^{-2}$.

The microstructures ascribed from the EBSD analyses unveil a definitive relationship between the carbon content and various attributes of the specimens. DT-1020, with its lowest carbon content, predominantly exhibits a (111) texture, an orientation naturally favored in BCC iron structures common to low-carbon steels. Transitioning to DT-1050, a combination of (101) and (110) orientations emerge. This amalgamation highlights the interplay of medium carbon content, facilitating varied deformation mechanisms and distinct recrystallization behaviors. The DT-1070 sample, characterized by the highest carbon content, prominently
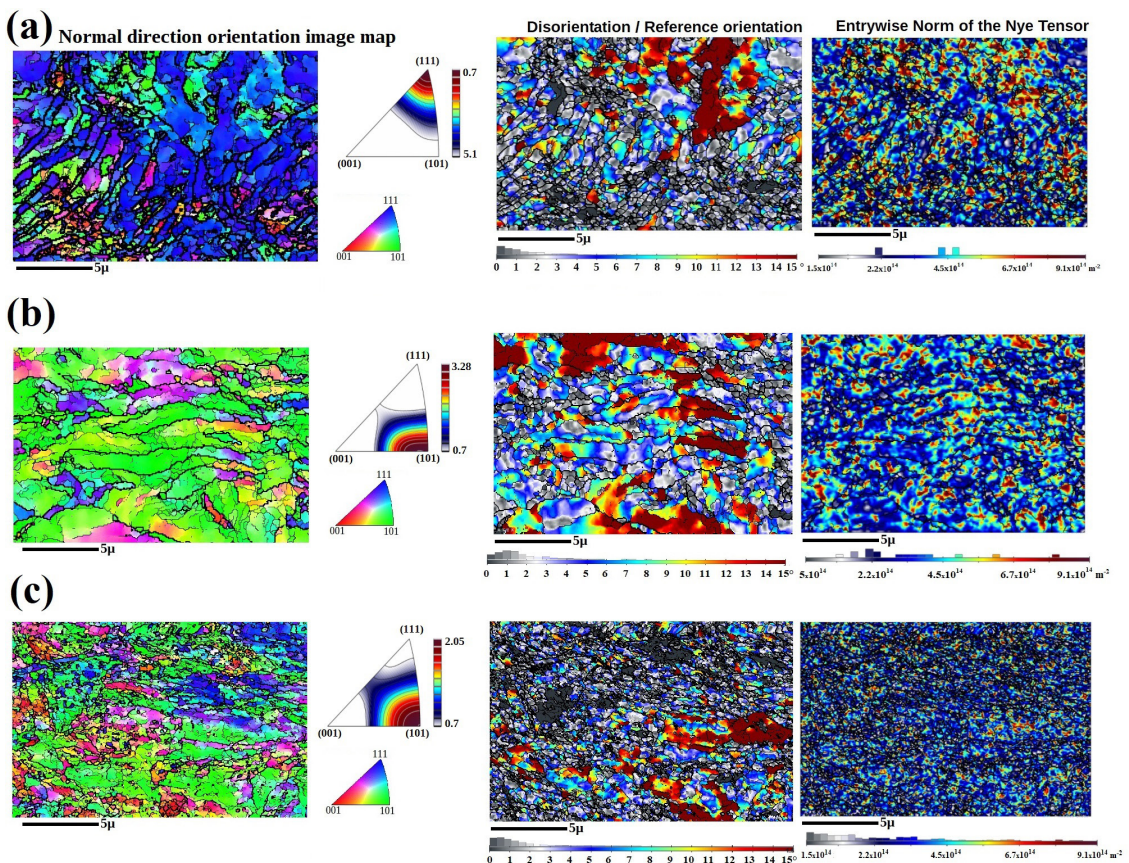


**Figure 2.** Normal direction orientation image (OIM), disorientation/reference orientation, and the Entrywise norm of the Nye tensor maps at ~20μm below the surface of the DT-1020 (a), DT-1050 (b), and DT-1070 (c) samples.

demonstrates the (101) texture. This orientation aligns with the most compact plane in the BCC structure, suggesting the sample enhanced ductility resultant from the higher carbon content facilitation of superior dislocation mobility. The dislocation density displays an evident gradient, escalating from DT-1020 to DT-1050. This progression highlights the heightened carbon content role in offering increased barriers to dislocation motion, consequently amplifying dislocation accumulation. However, the relative closeness in dislocation densities between DT-1050 and DT-1070 is an interesting observation. This suggests a saturation point in dislocation accumulation concerning the carbon content or an interplay of other microstructural variables. Considering the absence of cementite particle detection via conventional EBSD, it is assumed that their size must be ultra-fine. These minuscule cementite particles could act as potent barriers or pinning sites for dislocations, especially in higher carbon steels. Their presence or lack thereof could significantly influence the overall microstructural evolution post-treatment.

### 3.3.2. Mid-Thickness microstructure: Carbon effect on grain and dislocation

Figure 3 displays EBSD results taken from the med-thickness region of the DT-series specimens. The DT-1020 specimen has a marked prevalence of smaller recrystallized grains oriented in the (112) direction. Interestingly, the (110) grain

is a hotspot for intergranular distortion, with dislocation densities reaching a remarkable $9.1 \times 10^{16}$ m$^{-2}$. Contrarily, the recrystallized grains sit at a much lower $3.3 \times 10^{15}$ m$^{-2}$. Moving to the DT-1050 sample, elongated grains primarily aligned in the (111) direction become evident. Various factors, ranging from manufacturing-induced plastic deformation to directed grain growth, can account for this elongation. Notably, grains along this orientation also exhibit elevated storage energy, potentially fueling preferential grain growth. Lastly, DT-1070 showcases grains of impressive size, especially when juxtaposed against the other samples. These grains, attributed to manufacturing and post-process heat treatment, primarily exhibit (111) and (101) textures. Significant intragranular stress and a dislocation density nearing $9.0 \times 10^{16}$ m$^{-2}$ hint at possible structural vulnerabilities.

The EBSD results in the mid-thickness of investigated samples revealed intricate microstructural intricacies influenced by factors like manufacturing processes and carbon content. Comparatively, the DT-1020 sample, with its high dislocation density in the (110) grain, may suggest a lower carbon content that reduces the strength of steel, thereby increasing distortion. High dislocation density in the (110) grain can arise due to its crystallographic orientation favoring slip during deformation, coupled with interactions at grain boundaries where dislocations from neighboring grains accumulate. Additionally, the presence of obstacles, like hard phases
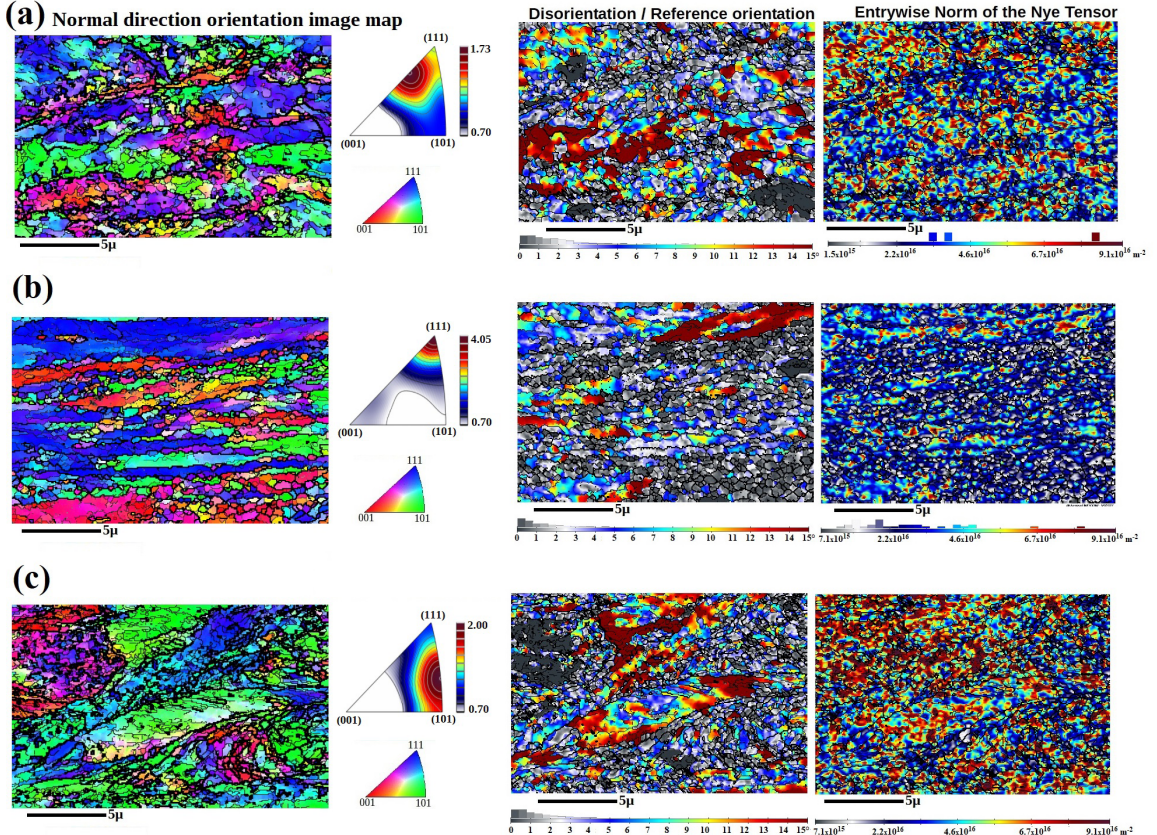


**Figure 3.** Normal direction orientation image (OIM), disorientation/reference orientation, and the Entrywise norm of the Nye tensor maps in the middle thickness of the DT-1020 (a), DT-1050 (b), and DT-1070 (c) samples.

within the (110) grain, can impede dislocation movement, leading to their pile-up and increased density. Meanwhile, the elongated grains of DT-1050, oriented predominantly in the (111) direction, could signify a moderate carbon content. This orientation often arises due to the balance between the inherent resistance provided by the carbon and the forces of manufacturing deformation[30,31]. It is worth noting that the increased storage energy in this grain orientation can be attributed to the carbon presence, which supports the structural stability. In contrast, DT-1070, with its coarse grains and dual texture orientation, possibly points towards a reduced carbon content. This could facilitate grain growth during heat treatment, although it leads to vulnerabilities in structural integrity. When contrasting these findings with the surface EBSD results from the earlier section, it is clear that the grain orientation, size, and associated dislocation densities shift in response to the carbon content across the sample depth.

### 3.3.3. Carbon and processing: Microstructural variations in dt specimens

Using point-to-point misorientation techniques, grain boundaries were classified based on misorientation angles. Low angle boundaries (LABs, $\Theta < 5°$) identified fully recrystallized grains, medium angle boundaries (MABs, $5° < \Theta < 15°$) indicated recovered or deformed grains, while high

angle boundaries (HABs, $\Theta > 15°$) marked grains with the highest internal energy, playing a crucial role in impeding dislocation movement and strengthening the material[21,32,33]. Figure 4a highlighted that DT-1070 exhibited the highest LABs in the near-surface area, while DT-1050 contained the largest fraction of HABs. Conversely, in the middle thickness, as shown in Figure 4c, DT-1020 led in LABs presence, and DT-1050 again dominated in HABs. Additionally, a minimal fraction of CSL (coincidence site lattice) boundaries were observed, aligning with expectations for a BCC-ferritic matrix. The Kernel Average Misorientation (KAM) distributions were examined at the near surface (Figure 4b) and middle thickness (Figure 4d). Grains were categorized based on their KAM values: fully recrystallized (KAM < 1°), partially recovered (1° ≤ KAM < 2°), and deformed (KAM > 2°)[31,34,35]. At the surface, DT-1070 displayed the largest fraction with KAM < 1°, whereas DT-1050 was characterized by the highest proportion of KAM > 2°. In the middle thickness region, DT-1050 had a significant dominance in KAM < 1° grains, while DT-1070 and DT-1020 had the most grains with KAM values exceeding 2°.

The variations in LABs, MABs, and HABs distributions across the DT-series specimens can be primarily attributed to their distinct carbon contents. The prominence of LABs in DT-1070 near the surface suggests a balance between the carbon content facilitating recrystallization and the effects of
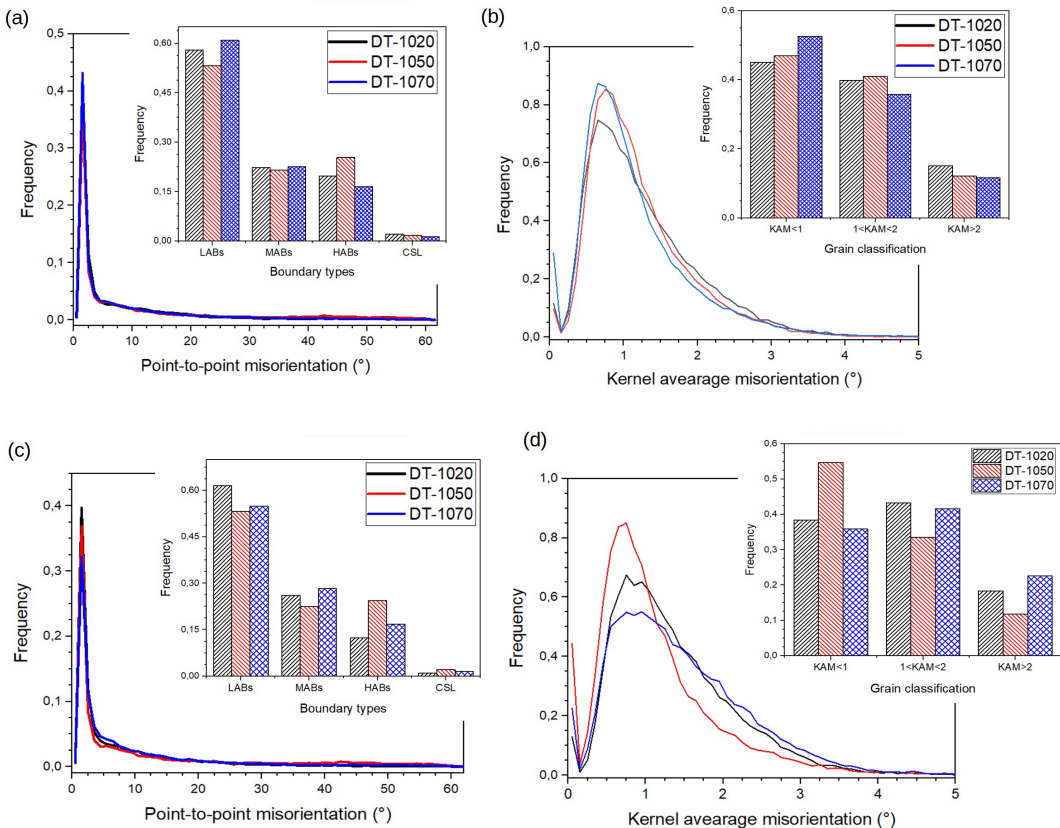


**Figure 4.** Comparative microstructural evaluations of DT-series specimens. Boundary classifications at the near-surface (a) and in the middle thickness (c). Moreover, the Kernel Average Misorientation (KAM) distributions near the surface (b) and at mid-thickness (d) of investigated specimens.

processing. The increased carbon content in DT-1070 could enhance the nucleation rate, thereby leading to higher LABs. On the other hand, the higher fraction of HABs in DT-1050, especially near the surface, suggests that the 0.5 wt% carbon facilitates greater misorientation during cold rolling and annealing, promoting more pronounced strengthening effects. The dominance of LABs in the middle thickness of DT-1020 may be attributed to the lower carbon content reducing the strength of the steel, thus intensifying distortion and promoting finer recrystallization. The consistently high HABs in DT-1050 across depths further underscore the significant role of its intermediate carbon content in offering a balanced response between deformation and recrystallization. The KAM distribution provides insights into the microstructural state post-deformation and subsequent annealing. DT-1070 higher fraction of fully recrystallized grains near the surface suggests that higher carbon steels potentially undergo rapid recrystallization[36]. Conversely, the pronounced fraction of deformed grains in DT-1050 may result from the unique interplay of deformation mechanisms enabled by its carbon content. These observations illustrate

the nuanced interplay of carbon content with processing techniques, offering a roadmap to manipulate microstructures for specific applications.

## 3.4. The role of carbon in DT samples: XRD insights

Figure 5 shows the X-ray diffraction (XRD) patterns for the DT-series samples: DT-1020, DT-1050, and DT-1070. Across all samples, the BCC-ferritic matrix is prominent, with the diffracted peaks corresponding to the (110), (200), and (211) planes. As the carbon content increases in the DT-1050 and DT-1070 specimens, additional peaks associated with cementite appear. However, these cementite peaks present low intensities. This subdued representation of cementite might result from their finer particulate nature, which could lead to lower XRD peak intensities. Table 2 presents the detailed X-ray diffraction data for the DT-series samples. Across the board, the 2theta values depict minor shifts in the diffraction angles, most notably with DT-1070 peak (200)α showing a slightly higher value. Variations in the Full Width at Half Maximum (FWHM) hint at changes in peak broadening, with DT-1050 revealing the broadest peak at (200)α and (211)α. In terms of lattice parameters, while the value of a remains relatively constant, b and c showcase minor differences, with DT-1070 exhibiting a slightly reduced 'a' value. Lattice distortion is highest for DT-1020 at 0.449% but notably decreases for DT-1070 to 0.291%. The dislocation density is highest in DT-1050, indicating a denser dislocation network than its counterparts. Lastly, microstrain remains fairly consistent across the series, although DT-1050 marginally stands out with a value of $0.146 \times 10^{-3}$.

The XRD patterns manifest subtle significant shifts in peak angles (2theta) and broadening (FWHM), each potentially indicative of underlying structural transformations and variations in microstructure as the carbon content increases. First, the incremental shift in the 2theta values, especially in the higher carbon variants DT-1050 and DT-1070, can be correlated with an alteration in the lattice parameters. The addition of carbon atoms in the BCC-ferritic matrix may lead to a slight distortion in the lattice. Even minor alterations in the atomic spacing or the insertion of carbon atoms could cause noticeable changes in the 2theta values.
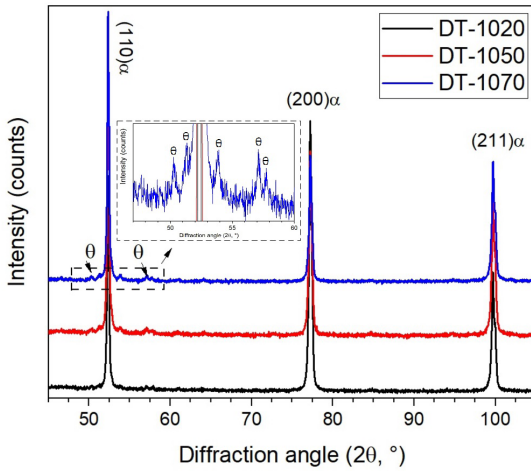


**Figure 5.** XRD patterns for the DT-series samples; DT-1020, DT-1050, and DT-1070.

**Table 2.** Detailed X-ray diffraction data analysis for the DT-series samples.

| | | DT-1020 | | DT-1050 | | DT-1070 | |
|---|---|---|---|---|---|---|---|
| Peak (110)α | 2theta (°) | 52.33968 | | 52.35248 | | 52.35407 | |
| | FWHM | 0.32093 | | 0.33565 | | 0.29821 | |
| Peak (200)α | 2theta (°) | 77.23934 | | 77.23468 | | 77.26809 | |
| | FWHM | 0.43985 | | 0.46890 | | 0.46985 | |
| Peak (211)α | 2theta (°) | 99.73737 | | 99.75456 | | 99.75263 | |
| | FWHM | 0.53321 | | 0.57034 | | 0.54935 | |
| Lattice parameters | a (Å) | 2.8664 | | 2.8664 | | 2.8654 | |
| | b (Å) | 2.8702 | 2.8650 ±0.0005 | 2.8688 | 2.8645 ±.0005 | 2.8698 | 2.8655 ±0.0005 |
| | c (Å) | 2.8582 | | 2.8581 | | 2.8611 | |
| Lattice distortion (%) | | 0.449 | | 0.422 | | 0.291 | |
| Average Dislocation density, ρ (m⁻²) | | 3.493E+12 | | 3.816E+12 | | 3.012E+12 | |
| Average microstrain (×10⁻³) | | 0.138 | | 0.146 | | 0.138 | |

Such shifts might imply the commencement of phase transformations or segregation of carbon atoms, leading to cementite formation[37].

Moreover, the broadening of XRD peaks, as represented by FWHM, is generally associated with various factors like grain size, lattice distortions, and the presence of microstrains[38,39]. The progressively higher FWHM values for DT-1050, especially for the $(200)\alpha$ and $(211)\alpha$ peaks, suggest increased lattice distortion or the presence of finer grains. The Debye–Scherer equation, which relates peak broadening to grain size, indicates that an increase in FWHM typically signifies a reduction in grain size[22,40]. As such, the higher carbon content might be refining the grain structure or enhancing the generation of defects, which can contribute to peak broadening.

Furthermore, the progressive carbon enrichment from DT-1020 to DT-1070 and the emergence of low-intensity cementite peaks, particularly in DT-1050 and DT-1070, highlight the role of carbon in microstructural evolution. The cementite, or Fe3C, typically forms platelets or lamellar structures during initial precipitation. However, with proper heat treatments or prolonged annealing, these can transform into spheroidized particles[41,42]. These spheroidized cementite particles are less detrimental to ductility than lamellar ones and can be responsible for improved strength. The fine nature of these cementite particles could be why their intensity is low in the XRD patterns. In addition, the increased carbon content in the steel compositions progressively strengthens the material[24]. Steels can strengthen through mechanisms such as grain refinement, solid solution strengthening, and precipitation hardening. Adding carbon can effectively hinder dislocation movement, a key mechanism in deformation. The carbon resultant "pinning" effect and fine spheroidized cementite particles can obstruct the dislocation pathways, thereby enhancing the strength[13,43]. Additionally, a denser dislocation network, as evidenced in DT-1050, further contributes to the strengthening effect.

## 3.5. Crystallographic texture variations in investigated samples

Figure 6 presents a visual representation of the orientation distribution function (ODF) at constant $\varphi_2$ values of 0° and 45°, offering insights into the crystallographic texture of the samples under consideration. The ODF, in essence, characterizes the distribution of crystallographic orientations in a polycrystalline material, enabling the identification of specific texture components represented as (hkl)[uvw]. Here, the (hkl) plane refers to the crystal plane that aligns parallel to the rolling plane (RP), while the [uvw] direction is the crystal direction that orients parallel to the rolling direction (RD)[17,44]. The samples under investigation all showcased the (001)[1-10], (001)[101], and (111)//ND – γ-fibre texture components. These components are commonly associated with samples that have undergone rolling and subsequent annealing, aligning with what is often observed in industrial steel production[1,45,46]. Intriguingly, the carbon content seems to play a role in altering texture intensity. For instance, the DT-1020 sample exhibited a texture intensity of 5.26, contrasting with the DT-1050 3.71 intensity, while DT-1070 recorded an intensity of 5.44. Diving deeper, the DT-1020 displayed distinguishable (111)[1-10] and (111)[0-11] components. On the other hand, the DT-1050 was marked by a pronounced (111)//ND – γ-fibre texture component. The DT-1070, on the contrary, showcased a variety of components, namely the (111)[1-10], (223)[1-10], and (111)[-1-12].

The crystallographic texture of the investigated steel samples reveals distinct texture components that emerge from cold rolling and annealing processes. Drawing from Ma et al.[47] observation, the presence of both <001> and <111> dual fiber texture structures in our samples suggests extensive strain conditions, which later influence the formation of the Cube component. The prevalence of these dual textures, combined with the insights from Dong's work[48], highlights the significant influence of continuous dynamic recrystallization in <001> grains and discontinuous dynamic recrystallization in <111> grains, elucidating the strong orientation dependence in the evolution of these textures. The varying intensities in DT-1020, DT-1050, and DT-1070, specifically the pronounced (111)//ND – γ-fiber texture in DT-1050, might be attributed to differing extents of DRX behaviors and grain boundary migrations during annealing.

Furthermore, drawing upon insights from Ravikiran et al.[49] and Sayyar et al.[50], the recrystallization behavior during annealing plays a pivotal role in determining the resulting texture. The presence of specific unfavorable components such as rotated-Goss (110)[110] and rotated-Cube (001)[110], as seen in some samples, can be linked to transformations that occur in the austenite temperature range, resulting from both recrystallization and shear deformation. The alterations in texture intensity based on carbon content, as observed across our samples, could manifest how carbon impedes or facilitates grain boundary migration and subsequent recrystallization events, as well as its influence on γ-fiber texture formation. With the deep drawability and formability implications of γ-fiber texture, as noted by Beladi et al.[51], understanding these texture evolutions is paramount for optimizing industrial steel production processes.

## 3.6. Tensile behavior of DT-Series Steels

Figure 7 and Table 3 delineate the engineering stress-strain curves for the investigated samples. The stress-strain curves of DT-1020 and DT-1070 steels exhibit a notable

**Table 3.** Mechanical properties obtained from the tensile test.

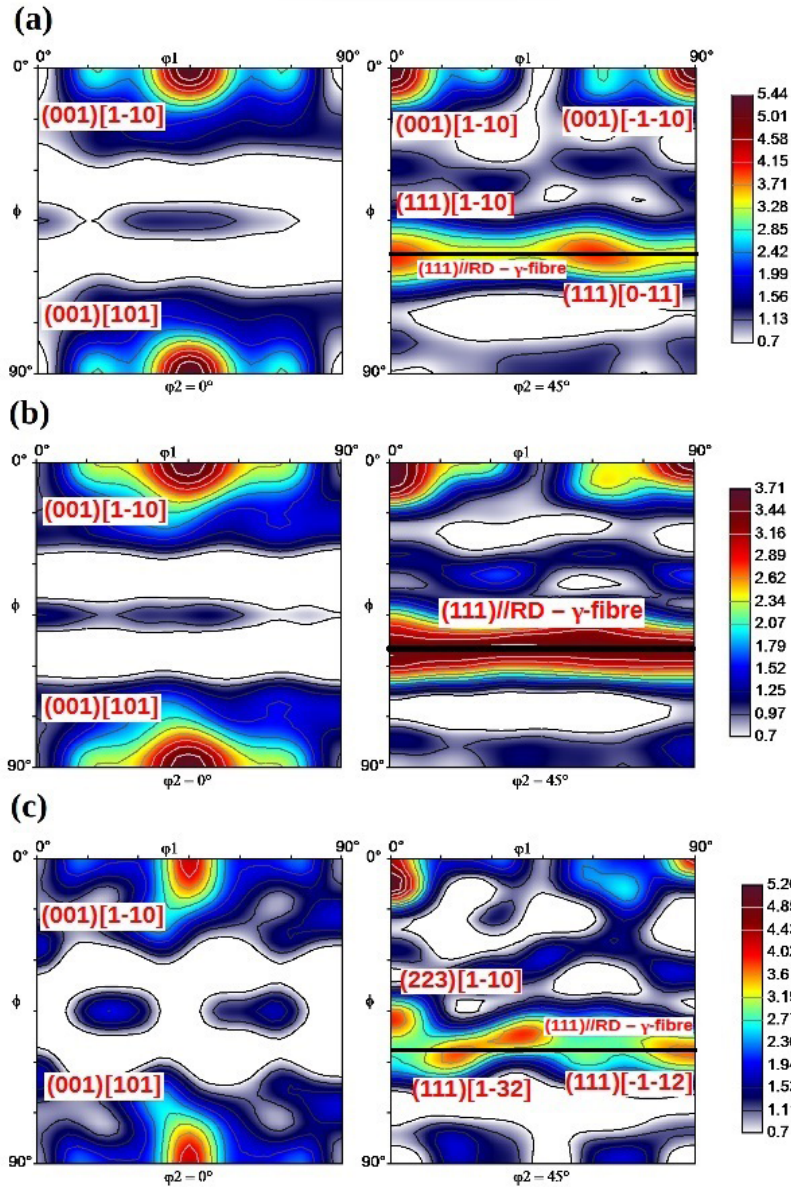| Specimens | Yield stress (YS, MPa) | Ultimate Tensile strength (UTS, MPa) | YS / UTS (%) | Total Elongation (mm/mm, %) | Area under curve (J/m³) |
|---|---|---|---|---|---|
| DT-1020 | 610 | 715 | 85.31 | 18.9 | 10442.3 |
| DT-1050 | 745 | 820 | 90.85 | 10.6 | 8305.8 |
| DT-1070 | 850 | 960 | 88.54 | 10.6 | 9543.2 |

**Figure 6.** ODFs at constant $\varphi_2$ values of 0° and 45° in the DT-series samples (a) DT-1020, (b) DT-1050, and (c) DT-1070.

dip immediately following the yielding point, attributable to phenomena such as Lüders banding or the yield point phenomenon[52], the Portevin-Le Chatelier (PLC) effect[53], and potential testing machine artifacts[54]. Lüders banding, occurring predominantly in BCC structures, leads to a temporary drop or plateau in the curve as the material undergoes plastic deformation without a corresponding increase in stress[52]. The PLC Effect, another strain-induced anomaly, results in serrations or dips in the curve due to dynamic strain aging. This effect may arise when diffusing atoms within the steel, like carbon or nitrogen, interact with dislocations under specific temperatures and strain rates. Furthermore, dips in the curve may not necessarily reflect the material properties but could instead stem from testing setup or procedural artifacts. Instances such as slack in the apparatus or abrupt
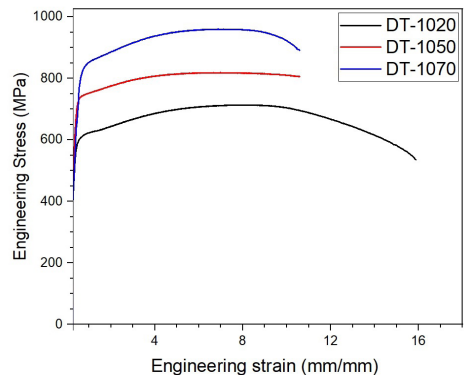


**Figure 7.** Engineering stress-strain curves for the investigated samples.

changes in strain rate, triggered by the machine response to yielding, can cause a momentary decrease in recorded stress.

The DT-1020 specimen showcased a yield stress (YS) of 610 MPa and an ultimate tensile strength (UTS) of 715 MPa, resulting in a YS/UTS ratio of 85.31% and a total elongation of 18.9% with an area under the curve amounting to 10442.3. The DT-1050 sample exhibited increased strengths with a YS of 745 MPa, a UTS of 820 MPa, and a YS/UTS ratio of 90.85%. However, it had a reduced total elongation of 10.6% and an area under the curve of 8305.8. The DT-1070 sample demonstrated the highest strengths, with a YS of 850 MPa and a UTS of 960 MPa. Its YS/UTS ratio stood at 88.54%, with a total elongation identical to DT-1050 at 10.6% but a notably larger area under the curve of 9543 $J/m^3$.

### 3.7. Microstructure, carbon, and mechanical behavior

The intricate relationship between the microstructure of steel and its mechanical properties has been the subject of extensive investigation. Beginning with the microstructural examination, SEM images unveiled the presence of spheroidized cementite in the samples. Per the literature, spheroidized cementite is often associated with enhanced ductility in steels[55,56], a trend evident in our study. For instance, the DT-1050 specimen, with its pronounced spheroidized cementite, displayed a reduction in elongation compared to DT-1020, possibly owing to the increased carbon content acting as a barrier to dislocation movement.

EBSD data further complements these findings. The dislocation density, often indicative of a material work-hardening capacity, showed a plausible correlation with the YS/UTS ratio of the samples. Higher dislocation densities typically signal a greater capacity for work hardening, increasing the YS/UTS ratio. The DT-1050 sample, with its higher carbon content, presented a higher YS/UTS ratio, suggesting increased work hardening, which aligns with the abovementioned concept. A heightened KAM often hints at a considerable density of low-angle grain boundaries, which are known to influence mechanical properties by impeding dislocation movement. Coupled with tensile test outcomes, it becomes evident that stored strain energy significantly contributes to the observed yield strength in our samples.

Furthermore, the variations in the crystallographic texture, especially the pronounced (111)//ND – γ-fiber texture in DT-1050, might influence the mechanical response during tensile testing. The dominant (111)//ND orientation, being the most densely packed, facilitates smoother slip mechanisms. This leads to enhanced ductility and work-hardening potential but could also lower the yield strength due to preferential slip along this plane. Specific texture components in industrial steel have been directly associated with rolling and annealing processes, which inherently affect mechanical behavior.

XRD analysis provided a quantitative measure of the phases present. Increased carbon content intensifies the prominence of phases that boost hardness, elucidating the hardness trends observed across DT-1020, DT-1050, and DT-1070. The tensile properties echo this trend, with higher carbon content specimens registering augmented yield and ultimate tensile strengths. In a novel revelation, the area under the stress-strain curve, representing the energy absorption

capacity, was found to be intricately tied to the carbon content and consequent microstructure. The DT-1070, with the highest carbon content, manifested the highest energy absorption. In contrast, the DT-1050, despite its higher strength attributes, displayed reduced energy absorption, suggesting a compromise between strength and ductility, a classic manifestation of the strength-ductility trade-off. This study sheds light on the nuanced interplay between microstructure, especially in the realm of EBSD findings and mechanical properties, offering valuable insights for industries aiming to refine steel production processes.

## 4. Conclusions

This investigation delves into the impact of spheroidizing cementite via cold-rolling and subsequent stress relief annealing on the microstructural characteristics and mechanical properties of commercial carbon steels, focusing on the interrelation between processing techniques, carbon content variations, and resultant steel behavior. The main conclusions are underscored by quantitative data, offering a detailed roadmap for steel property optimization through precise microstructural adjustments. Main conclusions supported by quantitative findings:

1.  The process notably enhances spheroidized cementite formation, particularly in high carbon content steel (Fe-0.7C wt%), where a significant increase in spheroidized structures was observed. This led to an improvement in ductility, with microhardness values showing a clear carbon content correlation: 28.0±1.0 HRC for DT-1020, 36.0±1.0 HRC for DT-1050, and 39.0±1.0 HRC for DT-1070.
2.  Carbon content critically influences texture evolution; DT-1020 primarily developed a (111) texture, whereas DT-1070 exhibited a refined (101) texture. This texture refinement with higher carbon content suggests enhanced dynamic recrystallization, affecting the material deformation and strain accommodation capabilities.
3.  EBSD analysis highlighted that DT-1050 displayed the highest dislocation density at approximately $7.8 \times 10^{16}$ $m^{-2}$ and varied misorientation gradients, with DT-1070 and DT-1020 showing significant increases in KAM values indicative of strain localization and enhanced plastic deformation capabilities.
4.  The tensile testing data revealed a direct relationship between carbon content and mechanical strength, with DT-1070 achieving the highest YS of 850 MPa and UTS of 960 MPa. In contrast, DT-1020 exhibited a lower YS of 610 MPa and UTS of 715 MPa, demonstrating the trade-off between strength and ductility across varying carbon contents.

## 5. Acknowledgments

Influence of Spheroidized Cementite on Ferritic Matrix Boundary Characteristics and Mechanical Behavior in Commercial Carbon Steels

13

# 6. References

1. Narayanswamy S, Saha R, Bhattacharjee PP. Cross-rolling mediated microstructure and texture evolution in severely cold-rolled and annealed ultrafine pearlite. Mater Charact. 2021;171:110751.

2. Furuhara T, Mizoguchi T, Maki T. Ultra-fine (α+ θ) duplex structure formed by cold rolling and annealing of pearlite. ISIJ Int. 2005;45(3):392-8.

3. Teixeira J, Moreno M, Allain SYP, Oberbillig C, Geandier G, Bonnet F. Intercritical annealing of cold-rolled ferrite-pearlite steel: microstructure evolutions and phase transformation kinetics. Acta Mater. 2021;212:116920.

4. Diao G, Yan Q, Shi X, Zhang X, Wen Z, Jin X. Improvement of wear resistance in ferrite-pearlite railway wheel steel via ferrite strengthening and cementite spheroidization. Mater Res Express. 2019;6(10):106513.

5. Amos PGK, Bhattacharya A, Nestler B, Ankit K. Mechanisms of pearlite spheroidization: insights from 3D phase-field simulations. Acta Mater. 2018;161:400-11.

6. Pereira HB, Echeverri EAA, Centeno DMA, Souza SS, Bauri LF, Manfrinato MD, et al. Effect of pearlitic and bainitic initial microstructure on cementite spheroidization in rail steels. J Mater Res Technol. 2023;23:1903-18.

7. Matusiewicz P, Augustyn-Nadzieja J, Czarski A, Skowronek T. Kinetics of pearlite spheroidization. Arch Metall Mater. 2017;62(1):231-4.

8. Caruso M, Godet S. Microstructural evolution during spheroidization annealing of eutectoid steel: effect of interlamellar spacing and cold working. Adv Mat Res. 2010;89-91:79-84.

9. Zhao Q-H, Jiang B, Wang J-M. Pearlite spheroidization mechanism and lifetime prediction of 12Cr1MoV steel used in power plant. In 4th Annual International Conference on Material Science and Engineering (ICMSE 2016); 2016; Guangzhou, China. Proceedings. Paris: Atlantis Press; 2016. p. 195-201.

10. Zhu Q, Chen J, Gou G, Chen H, Li P. Ameliorated longitudinal critically refracted: attenuation velocity method for welding residual stress measurement. J Mater Process Technol. 2017;246:267-75.

11. Wang H, Wang F, Qian D, Chen F, Dong Z, Hua L. Investigation of damage mechanisms related to microstructural features of ferrite-cementite steels via experiments and multiscale simulations. Int J Plast. 2023;170:103745.

12. Fu ZH, Yang BJ, Shan ML, Li T, Zhu ZY, Ma CP, et al. Hydrogen embrittlement behavior of SUS301L-MT stainless steel laser-arc hybrid welded joint localized zones. Corros Sci. 2020;164:108337.

13. Liu H, Wei J, Dong J, Dong. Comprehensive improvement of corrosion resistance and strength of ferrite-pearlite low alloy steel by cementite spheroidization treatment. J Mater Res Technol. 2023;23:1618-29.

14. Kim KS, Wi DY, Lee JS, Lee KA. Adjusting the thermomechanical condition to change the microstructure of C–Mn cold heading quality steel for rapid cementite spheroidization at subcritical temperature: effect of stored energy. Metall Mater Trans, A Phys Metall Mater Sci. 2022;53(3):1099-109.

15. Caruso M, Godet S. Microstructural evolution during spheroidization annealing of eutectoid steel: effect of interlamellar spacing and cold working. Adv Mat Res. 2014;89-91:79.

16. Beausir B, Fundenberger JJ. Analysis tools for electron and X-ray diffraction, ATEX [software]. Metz: Université de Lorraine; 2017 [cited 2023 Nov 13]. Available from: www.atex-software.eu

17. Cullity B. Elements of X-RAY diffraction. 2nd ed. Notre Dame: University of Notre Dame; 1994.

18. Holzwarth U, Gibson N. The Scherrer equation versus the "Debye-Scherrer equation". Nat Nanotechnol. 2011;6(9):534.

19. Karoui H, Riffault B, Jeannin M, Kahoul A, Gil O, Ben Amor M, et al. Electrochemical scaling of stainless steel in artificial seawater: Role of experimental conditions on $CaCO_3$ and $Mg(OH)_2$ formation. Desalination. 2013;311:234-40.

20. Pinheiro PH, Masoumi M, Herculano LFG, Xavier JVB, de Lima SKB, Silva ES, et al. Microstructural and Texture evolution of pearlite-drawn wires for flexible marine pipelines: investigating the effect of heat treatments on mechanical properties. Metals. 2023;13(4):805.

21. Ramirez MFG, Hernández JWC, Ladino DH, Masoumi M, Goldenstein H. Effects of different cooling rates on the microstructure, crystallographic features, and hydrogen induced cracking of API X80 pipeline steel. J Mater Res Technol. 2021;14:1848-61.

22. Kotresh MG, Patil MK, Sunilkumar A, Sushilabai A, Inamdar SR. A study on the effect of reaction temperature on the synthesis of magnesium hydroxide nanoparticles: comparative evaluation of microstructure parameters and optical properties. Results Opt. 2023;10:100336.

23. DIN: Deutsches Institut für Normung. DIN EN 6892-1. Berlin.

24. Li YJ, Choi P, Goto S, Borchers C, Raabe D, Kirchheim R. Evolution of strength and microstructure during annealing of heavily cold-drawn 6.3 GPa hypereutectoid pearlitic steel wire. Acta Mater. 2012;60(9):4005-16.

25. Lee JW, Lee JC, Lee YS, Park KT, Nam WJ. Effects of post-deformation annealing conditions on the behavior of lamellar cementite and the occurrence of delamination in cold drawn steel wires. J Mater Process Technol. 2009;209(12-13):5300-4.

26. Morsdorf L, Emelina E, Gault B, Herbig M, Tasan CC. Carbon redistribution in quenched and tempered lath martensite. Acta Mater. 2021;205:116521.

27. Zhao TZ, Zhang SH, Zhang GL, Song HW, Cheng M. Hardening and softening mechanisms of pearlitic steel wire under torsion. Mater Des. 2014;59:397-405.

28. Xiong Z, Timokhina I, Pereloma E. Clustering, nano-scale precipitation and strengthening of steels. Prog Mater Sci. 2021;118:100764.

29. Li W, Liu H, Zhu J, Zhang X, Li G, Li Y, et al. Efficient photocathodic protection of nanoflower $MgIn_2S_4$-modified CNNs composites on 316 SS under visible light. Mater Res Bull. 2024;173:112694.

30. Karaman I, Sehitoglu H, Gall K, Chumlyakov YI. On the deformation mechanisms in single crystal hadfield manganese steels. Scr Mater. 1998;38(6):1009-15.

31. Masoumi M, Silva CC, de Abreu HFG. Effect of crystallographic orientations on the hydrogen-induced cracking resistance improvement of API 5L X70 pipeline steel under various thermomechanical processing. Corros Sci. 2016;111:121-31.

32. Mohtadi-Bonab MA, Ariza EA, Loureiro RCP, Centeno D, Carvalho FM, Avila JA, et al. Improvement of tensile properties by controlling the microstructure and crystallographic data in commercial pearlitic carbon-silicon steel via quenching and partitioning (Q&P) process. J Mater Res Technol. 2023;23:845-58.

33. Masoumi M, Abreu HFG, Herculano LFG, Pardal JM, Tavares SSM, Silva MJG. EBSD study of early fractured phenomena in a 350 grade Maraging steel elbows exposed to hydrofluoric acid. Eng Fail Anal. 2019;104:379-87.

34. Masoumi M, Silva CC, de Abreu HFG. Effect of crystallographic orientations on the hydrogen-induced cracking resistance improvement of API 5L X70 pipeline steel under various thermomechanical processing. Corros Sci. 2016;111:121-31.

35. Masoumi M, Abreu HFG, Herculano LFG, Pardal JM, Tavares SSM, Silva MJG. EBSD study of early fractured phenomena in a 350 grade Maraging steel elbows exposed to hydrofluoric acid. Eng Fail Anal. 2019;104:379-87.

36. Hurley PJ, Hodgson PD. Formation of ultra-fine ferrite in hot rolled strip: potential mechanism for grain refinement. Mater Sci Eng A. 2001;302(2):206-14.

37. Kim B, Celada C, San Martín D, Sourmail T, Rivera-Díaz-Del-Castillo PEJ. The effect of silicon on the nanoprecipitation of cementite. Acta Mater. 2013;61(18):6983-92.

38. Khedr M, Li W, Min N, Liu W, Jin X. Effects of increasing the strain rate on mechanical twinning and dynamic strain aging in Fe-12.5Mn-1.1C and Fe–24Mn-0.45C–2Al austenitic steels. Mater Sci Eng A. 2022;842:143024.

39. Masumura T, Inami K, Matsuda K, Tsuchiyama T, Nanba S, Kitahara A. Quantitative evaluation of dislocation density in as-quenched martensite with tetragonality by X-ray line profile analysis in a medium-carbon steel. Acta Mater. 2022;234:118052.

40. Basak M, Rahman L, Ahmed F, Biswas B, Sharmin N. The use of X-ray Diffraction peak profile analysis to determine the structural parameters of cobalt ferrite nanoparticles using Debye-Scherrer, Williamson-Hall, Halder-Wagner and Size-strain plot: different precipitating agent approach. J Alloys Compd. 2021;9:127248.

41. Syn CK, Lesuer DR, Sherby OD. Influence of Microstructure on tensile properties of spheroidized ultrahigh-carbon (1.8 Pct C) steel. Metall Mater Trans, A Phys Metall Mater Sci. 1994;25(7):1481-93.

42. Kumar S, Samanta S, Singh SB. An alternative quenching and partitioning (Q&P) process via spheroidization. Mater Charact. 2022;191:112049.

43. Pereira HB, Alves LHD, Rezende AB, Mei PR, Goldenstein H. Influence of the microstructure on the rolling contact fatigue of rail steel: spheroidized pearlite and fully pearlitic microstructure analysis. Wear. 2022;498-499:204299.

44. Schwartz A, Kumar M, Adams B, Field D. Electron backscatter diffraction in materials science. 2nd ed. New York: Springer; 2011.

45. Großterlinden R, Imlau KP, Kawalla R, Lotter U, Reip CP. Possible influences on textures in unalloyed steels and their effects on steel properties. Steel Res. 1996;67(10):456-63.

46. Ravikiran K, Li L, Lehnhoff G, Sharma NK, Kannan R, Saini N, et al. Microstructure and crystallographic texture of high frequency electric resistance welded X65 pipeline steel. Mater Chem Phys. 2023;302:127758.

47. Ma H, Zeng W, Kou Y, Zhang P, Zhang F, Liang X. Formation mechanism of Cube texture components ({001}<100>) associated with dynamic recrystallization during compression in the single BCC phase region of Ti-22Al-25Nb alloy. J Alloys Compd. 2023;966:171563.

48. Dong Y, Liu X, Xu H, He Y, Ke Y, Zhang W. Relationship between β→α dynamic transformation and dynamic recrystallization under thermomechanical coupling in Ti-5Al-5Mo-5V-1Cr-1Fe alloy. J Mater Sci Technol. 2024;179:98-113.

49. Ravikiran K, Li L, Lehnhoff G, Sharma NK, Kannan R, Saini N, et al. Microstructure and crystallographic texture of high frequency electric resistance welded X65 pipeline steel. Mater Chem Phys. 2023;302:127758.

50. Sayyar N, Hansen V, Tucho WM, Minde MW. Directed laser deposition of super duplex stainless steel: Microstructure, texture evolution, and mechanical properties. Heliyon. 2023;9(4):e15144.

51. Beladi H, Tari V, Rollett AD, Rohrer GS. The influence of γ-fibre texture on the grain boundary character distribution of an IF-steel. Scr Mater. 2023;222:115042.

52. Mao W, Gao S, Gong W, Harjo S, Kawasaki T, Tsuji N. Quantitatively evaluating the huge Lüders band deformation in an ultrafine grain stainless steel by combining in situ neutron diffraction and digital image correlation analysis. Scr Mater. 2023;235:115642.

53. Ren SC, Morgeneyer TF, Mazière M, Forest S, Rousselier G. Effect of Lüders and Portevin-Le Chatelier localization bands on plasticity and fracture of notched steel specimens studied by DIC and FE simulations. Int J Plast. 2021;136:102880.

54. Njiti MM, Osman ND, Mansor MS, Rabaiee NA, Abdul Aziz MZ. Potential of Metal Artifact Reduction (MAR) and Deep Learning-based Reconstruction (DLR) algorithms integration in CT Metal artifact correction: a review. Radiat Phys Chem. 2024;218:111541.

55. Prasad C, Bhuyan P, Kaithwas C, Saha R, Mandal S. Microstructure engineering by dispersing nano-spheroid cementite in ultra fine-grained ferrite and its implications on strength-ductility relationship in high carbon steel. Mater Des. 2018;139:324-35.

56. Liu G, Zhang M, Feng Y, Cao K, Li S, Wang Y. Influence of warm rolling temperature on multi-scale lamellar structure and mechanical properties of medium carbon steel. J Mater Res Technol. 2022;18:3739-50.